Whistler Mode Wave-Driven Electron Scattering Properties from ELFIN Measurements of the Precipitation Ratio

Xiao-Chen Shen[1], Wen Li[1], Qianli Ma[1,2], Murong Qin[1], Luisa Capannolo[1], Miroslav Hanzelka[1,3,4], Vassilis Angelopoulos[5], Anton V. Artemyev[5], Colin Wilkins[5], Jiang Liu[5], and Ethan Tsai[5]

[1] Center for Space Physics, Boston University, Boston, MA, USA

[2] Department of Atmospheric and Oceanic Sciences, University of California, Los Angeles, CA, USA

[3] GFZ German Research Centre for Geosciences, Potsdam, Germany

[4] Department of Space Physics, Institute of Atmospheric Physics of the Czech Academy of Sciences, Prague, Czechia

[5] Department of Earth, Planetary, and Space Sciences, UCLA, Los Angeles, CA, USA

Corresponding authors:

Xiao-Chen Shen (sdusxc@gmail.com)

Key Points:

- Properties of electron scattering driven by whistler waves are revealed from ELFIN measurements of precipitation ratio
- This precipitation efficiently extends to high energies when the 63 keV electron precipitation ratio becomes large especially on dayside
- Strong precipitation at ~63 keV correlates with active geomagnetic levels and is concentrated over the midnight-dawn-noon sector at L>5

Abstract

Whistler-mode chorus and hiss waves play an important role in Earth's radiation belt electron dynamics. Direct measurements of whistler wave-driven electron precipitation and the resultant pitch angle distribution were previously limited by the insufficient resolution of low Earth orbit satellites. In this study, we use recent measurements from the Electron Losses and Fields INvestigation (ELFIN) CubeSats, which provide energy- and pitch angle-resolved electron distributions to statistically evaluate electron scattering properties driven by whistler waves. Our survey indicates that events with increasing precipitating-to-trapped flux ratios (evaluated at 63 keV unless otherwise specified) correlate with increasing trapped flux at energies up to ~750 keV. Weak precipitation events (precipitation ratio <0.2) are evenly distributed, while stronger precipitation events tend to be concentrated at L>5 over midnight-to-noon local times during disturbed geomagnetic conditions. These results are crucial for characterizing the whistler-mode wave driven electron scattering properties and evaluating its impact on the ionosphere.

Plain Language Summary

Chorus and hiss are two key whistler-mode electromagnetic waves in Earth's magnetosphere that interact with trapped energetic electrons, scattering them into the upper atmosphere. However, previous satellites at low Earth orbit (LEO) had limited resolution in measuring electron pitch angle (the angle between the electron velocity and the magnetic field) and energy, making it challenging to fully understand whistler wave-driven electron precipitation properties. In this study, we use recently acquired measurements from Electron Losses and Fields INvestigation (ELFIN) CubeSats, which provide full electron energy and pitch angle distributions from LEO, to statistically evaluate whistler wave-driven electron precipitation properties. We sort the identified events by the precipitation ratio (the ratio of the precipitating to trapped flux). Our results indicate that (a) events with large precipitation ratios correlate with increased trapped flux, indicating highly efficient electron precipitation; (b) dayside precipitation occurs at higher energies compared to nightside precipitation; (c) small ratio events distribute evenly across local times, while large ratio events tend to be concentrated at large distances from midnight to noon local times, particularly during more intense geomagnetic activities. These findings are critical for characterizing the electron scattering and precipitation properties and assessing their impact on the ionosphere.

1 Introduction

Whistler mode chorus and hiss waves are right-hand polarized electromagnetic emissions typically observed outside and inside the plasmasphere, respectively (e.g., Agapitov et al., 2018; Aryan et al., 2022; W. Li et al., 2009; Meredith et al., 2012, 2018, 2021). Chorus waves are discrete and coherent emissions with frequencies over 0.1–0.8 f_{ce} (f_{ce} denotes the electron cyclotron frequency) and normally have a gap near 0.5 f_{ce} likely due to Landau damping (J. Li et al., 2019) separating them into lower (< $0.5f_{ce}$) and upper (> $0.5f_{ce}$) bands. The typical scale size of chorus waves is several hundred kilometers as determined from multi-satellite observations (Agapitov et al., 2017; Shen et al., 2019; S. Zhang et al., 2021). Chorus wave distributions exhibit a strong dependence on geomagnetic conditions, as electron injection during substorms is an important source of chorus waves (Meredith et al., 2001, 2020). Hiss waves are broadband incoherent emissions with frequencies over 20–2000 Hz (W. Li et al., 2013b; Meredith et al., 2018). Sources of hiss waves in Earth's magnetosphere are complex and include propagation from chorus waves and/or lightning-generated whistler waves, and local generation due to plasma instabilities (Bortnik et al., 2008, 2009; Chen et al., 2012; Draganov et al., 1992; He et al., 2019, 2020; Kim et al., 2015; W. Li et al., 2013b; Meredith et al., 2006). Hiss waves are mostly observed inside the plasmasphere with an average wave amplitude of tens of pT on the dayside (Malaspina et al., 2016, 2017; Meredith et al., 2018). Large amplitude hiss waves tend to be observed close to the plasmapause or in plumes from the post-midnight to the noon sector during geomagnetically active periods (Shen et al., 2024).

Both chorus and hiss waves play an important role in scattering energetic electrons, ranging from several keV to hundreds of keV, into the loss cone through resonant interactions. Subsequently, these electrons precipitate into the Earth's atmosphere, potentially contributing to electron microbursts (Breneman et al., 2017; Chen et al., 2021, 2022; Shumko et al., 2018) and the formation of pulsating and diffuse auroras (e.g., Bortnik & Thorne, 2007; Horne & Thorne, 2003; W. Li et al., 2014, 2019; Ma et al., 2020, 2021, 2022; Ni et al., 2008, 2014b; Nishimura et al., 2010; Ozaki et al., 2018; Shen et al., 2023). Moreover, electron precipitation observed by multiple NOAA POES satellites has been used to infer the global distribution of chorus waves (W. Li et al., 2013a).

Although electron precipitation driven by chorus and hiss waves has been extensively studied (Bortnik & Thorne, 2007; H. Li et al., 2016; W. Li et al., 2014, 2019; Ma et al., 2020, 2021; Ozaki et al., 2019), high resolution electron measurements in both energy and pitch angle remain limited. In particular, a systematic analysis of pitch angle and energy-resolved electron precipitation distribution driven by whistler waves, directly measured at low altitudes, is still lacking. In this study, we utilize electron pitch angle and energy distributions recently measured by the Electron Losses and Fields INvestigation (ELFIN) CubeSats (2019-2022) to evaluate the detailed properties of whistler wave-driven electron precipitation into the Earth's upper atmosphere.

2 Dataset and Event Analysis

We use electron measurements from the Energetic Particle Detector for Electrons (EPDE) onboard the dual-CubeSat ELFIN mission (Angelopoulos et al., 2020). ELFIN was launched on September 15, 2018 into a Low Earth Orbit (LEO) at ~450 km altitude with an orbital period of ~90 minutes. The EPDE instrument provides differential electron flux in 16 energy channels from ~50 keV up to 6 MeV. The pitch angle is resolved by computing the angle between the detector's look direction and the magnetic field orientation from the IGRF model. Full pitch angle coverage is obtained in each half spin (~1.5 s). We bin ELFIN measurements in each half spin period to obtain the electron pitch angle distribution. The measurement from the EPDE electron detector is considered as saturated when total electron counts in all energy channels goes above 130k/s. These events often occur during large ratio electron precipitation events with a precipitation ratio around or above one (X.-J. Zhang et al., 2022). In this study, we have excluded saturated events and are not focusing on electron precipitation events with a precipitation ratio close or even larger than one. Therefore, our results are not affected by saturation events. A visual inspection is applied to remove data periods when the phase angle (the angle between the detector and the background magnetic field) is not well resolved or with contamination from solar energetic proton events. Additionally, the geomagnetic Auroral Electrojet (AE) index is used to evaluate the dependence of whistler wave-driven electron precipitation events on geomagnetic activity.

Figure 1 shows an example of ELFIN measurements of energetic electron distributions at low altitudes on January 27, 2021. During the event, the solar wind dynamic pressure (Figure 1a, black) remained low and relatively stable from 1 to 1.5 nPa for at least three hours before the ELFIN measurements (~1820 UT; marked by two dashed vertical red lines in Figures 1a–1b). The interplanetary magnetic field (IMF) B_z component in Geocentric Solar Magnetospheric (GSM) coordinates (Figure 1a, red) was negative and turned to values close to zero ~80 minutes prior to the ELFIN observations. A moderate substorm occurred with AE* (the maximum AE during the preceding three hours) reaching up to ~500 nT (Figure 1b).

Within ~4.5 minutes, from 18:17:30 to 18:23:00 UT, ELFIN-A traveled from L ~3.5 to L ~7, providing electron pitch angle measurements at various energies (Figures 1c–1d) across the outer radiation belt. Starting from ~18:19:40 UT, a significant electron flux intensification is observed for both trapped (near 90°) and precipitating (within the local loss cone close to 180°) electrons. These electron flux enhancements are observed until L~6.4 and are more intense at tens of keV energy channels than at hundreds of keV energy channels (Figures 1c–1d). In each half-spin, the ELFIN CubeSat can measure a full range of pitch angles. During each half-spin, the average flux in the local loss cone, precipitating into the Earth's upper atmosphere, is calculated as the average flux inside the loss cone; the average flux locally trapped between the loss cone and the anti-loss cone is calculated as the average flux outside the loss cone. Two bins very close to the local loss cone are excluded in the calculation to reduce the influence of uncertainties in determining the realistic loss cone. The bounce loss cone is estimated from the IGRF model by assuming particles to be lost at 100 km above the Earth surface. The loss cone angle at the ELFIN altitudes is nearly constant around 67°. By calculating the average energy flux outside and inside the loss cone (refers to the half-bounce loss cone in this study) respectively, locally trapped and precipitating energy fluxes are shown in Figures 1e–1f. Energy spectrograms of trapped and precipitating electrons show that during the period of enhanced electron flux, the energy flux of electrons from tens of keV up to < 1 MeV increases significantly. The precipitation ratio, which is the ratio between precipitating and trapped electron energy flux (Figure 1g), exhibits a value close to 1 during several strong flux enhancements at low energies (from 18:19:40 to 18:20:50 UT). A value close to one indicates a full loss cone (i.e., strong pitch angle diffusion). This electron precipitation is suggested to be primarily caused by pitch angle diffusion by whistler mode waves near the magnetic equator. Whistler mode chorus wave is not prominent on the dusk side near MLT~18 at L~4.8, while whistler mode hiss and plume hiss are more frequently occurring in this region (Meredith et al., 2021). Plasmaspheric hiss and plume hiss are typically present on the dayside and duskside especially when the plasmasphere expands (Meredith et al., 2021; W. Zhang et al., 2019). Both chorus and hiss waves drive electron precipitation with a similar energy spectrum in the regions of interest, peaking at tens of keV and decreasing with increasing energy (Shen et al., 2023). At L < 3, the peak energy of electron precipitation driven by hiss typically occurs at hundreds of keV, which is the main cause of the energy and L dependent slot region and the bump-on-tail electron distribution (Claudepierre et al., 2019; Ma et al., 2016; Zhao et al., 2019). From ELFIN measurements, electron precipitation driven by chorus and hiss cannot be well separated. Therefore, in this study, we present precipitation properties from the combined effects of chorus and hiss waves.

Electron precipitation driven by electromagnetic ion cyclotron (EMIC) waves peaks at relativistic energies (Angelopoulos et al., 2023; Blum et al., 2015; Capannolo et al., 2022, 2023; Jordanova et al., 2008; Miyoshi et al., 2008; Omura & Zhao, 2012; Qin et al., 2018, 2020; X.-J.

Zhang et al., 2021) and can extend to subrelativistic electrons (Capannolo et al., 2018, 2019), potentially/partially due to nonresonant wave-particle interactions (An et al., 2022; Chen et al., 2016). We require the peak precipitation ratio to be at energy below 100 keV to exclude EMIC-driven precipitation. Current sheet scattering (CSS) is mostly observed on the nightside, exhibiting an energy dispersion feature along the L shell: higher energy precipitation occurs at lower L shells, while lower energy precipitation occurs at higher L shells (Haiducek et al., 2019; Sergeev et al., 1983; Wilkins et al., 2023; Yue et al., 2014). We restrict our analysis to $3 < L < 8$, covering the outer radiation belt and require the minimum energy flux of 300 keV trapped electrons to be greater than 10^6 keV/(s·sr·cm^2·MeV) to ensure that the measurements are within the outer radiation belt with sufficient high-energy electron fluxes. This selected threshold is validated through visual inspections. Note that the median energy flux of 300 keV trapped electrons measured near the equator at L~5 (L~3) is around 10^9 (10^7) keV/(s·sr·cm^2·MeV) by Van Allen Probes (Shen et al., 2017). By incorporating the criterion mentioned above, which stipulates that the peak precipitation ratio should be below 100 keV, CSS-driven precipitation is excluded.

We apply these selection criteria to ELFIN measurements between 2019 and 2022 to obtain statistical properties of whistler-mode wave-driven electron precipitation in the following section.

3 Statistical Results

3.1 Pitch Angle Distribution

We record the electron pitch angle distribution measured by ELFIN from ~50 keV to 6 MeV during selected whistler wave-driven precipitation events. The pitch angle along a single look direction changes with the spacecraft's spin. The changing rate of pitch angle depends on the angle between the spin plane and the background magnetic field direction. To obtain an unbiased dataset due to the inclusion of different samples of events, in each half spin (from the smallest to the largest pitch angle), we linearly interpolate the observed electron flux on a logarithmic scale onto the pitch angle grids to be used for our following statistical analyses. We also require that each half spin measurements cover pitch angles at least from 30° to 150°. Therefore, all selected events (half spin measurements) are included in each pitch angle bin and included only once. We flipped pitch angles observed in the southern hemisphere so that a pitch angle close to 0° (180°) points towards the loss cone (anti-loss cone).

Figures 2a–2d show the median electron energy flux as a function of pitch angle sorted by the precipitation ratio at multiple energies over 63–753 keV. As the loss cone fills up (i.e., from small to large precipitation ratios), there is a continuous trend of increasing trapped flux, resulting in highly efficient electron precipitation into the loss cone during large precipitation ratio events. This trend is observed for all the energy channels and is most significant at 63 keV, which shows around one order of magnitude stronger precipitating flux during large precipitation ratio events (> 0.7) than those during small ratio events (0.1–0.2). Figures 2e–2h show the normalized distribution by the energy flux at the 90° pitch angle. It shows that events with a larger precipitation ratio can extend to significantly higher energies (at least 520 keV), though the high-energy precipitation is less efficient. These results highlight the importance of large ratio events, likely driven by intense whistler waves, in filling the loss cone at low energies and extending to higher energies. Electrons at > 90° pitch angles are mirroring back to the equator. Overfilling events with a precipitation ratio greater than one, which might be caused by nonlinear wave-particle interactions between electrons and oblique chorus waves (X.-J. Zhang et al., 2022), are included in the category of precipitation ratio > 0.7.

3.2 Correlation Between Electron Precipitation Ratio at 63 keV and Higher Energies

We evaluate the correlation between the precipitation ratio at 63 keV and that at higher energies to further examine how the precipitation ratio changes from tens of keV to hundreds of keV. Figure 3a shows an example of the analysis at MLT ~14 h. The precipitation ratio at 183 keV increases as the precipitation ratio at 63 keV increases. Based on the quasi-linear theory, electron precipitation ratio can be estimated (Ni et al., 2014b) as following

$$\chi(E) = \frac{2\int_0^1 I_0[Z_0(E)\tau]\cdot\tau\cdot d\tau}{I_0[Z_0(E)]}, \quad (1)$$

where I_0 is the modified Bessel function of the first kind, $Z_0 = \sqrt{\frac{D_{SD}}{(<D_{\alpha\alpha}>|_{LC})}}$ is the square root of the ratio of strong diffusion limit and pitch angle diffusion rate at the loss cone, and τ is an integration variable. For a given dipole L shell, D_{SD} is fixed and the precipitation ratio only depends on the $< D_{\alpha\alpha} > |_{LC}$ for various energies. Therefore, the ratio of precipitation between different energy channels only depends on the $< D_{\alpha\alpha} > |_{LC}$ of these two energy channels and can be explicitly calculated (Figure 4). The calculated relation between precipitation ratios of 63 keV and higher energy electrons indicates that although the relation of precipitation ratios at two energies exhibits an exponential-like dependence on the precipitation ratio, a linear approach is well enough to capture this relation at a precipitation ratio of 63 keV electrons < 0.8. In this work, we therefore use linear fitting to precipitation ratios below 0.8 to simplify the process to compare the efficiencies of extending to higher energies for the studied categories. We can reasonably assume that the precipitation ratio at 183 keV decreases to zero when the ratio at 63 keV is zero. The red line in Figure 3a represents the fitted line to the observations, with a slope k=0.49. Figure 3b is another example of the fitting analysis applied to a higher energy channel at 520 keV. We apply this analysis to multiple energies and MLTs, and obtain k values as a function of energy and MLT, as shown in Figure 3c. The slope k decreases with increasing energy, indicating that the whistler-mode wave-driven precipitation ratio decreases with increasing energy above 63 keV, as also expected from quasi-linear theory. More interestingly, it shows that the slope k is larger on the dayside (6 < MLT < 18) for energies up to 500 keV. Electrons at > 700 keV are not always observed, thus potentially resulting in a large uncertainty in the statistical values. This suggests that dayside whistler-mode waves result in a harder energy spectrum of electron precipitation ratio compared to other local times, possibly due to the dependence of the latitudinal extent of whistler waves on MLT. Previous statistical surveys indicate that dayside whistler-mode waves can extend to higher latitudes (Agapitov et al., 2018; W. Li et al., 2009; Meredith et al., 2012, 2021), driving higher-energy electron precipitation due to the increased minimum resonant energy. In addition to the precipitation ratio, the energy spectrum of trapped energetic electron fluxes at the equator is harder on the dayside than on the nightside due to electron drift and pitch angle scattering loss (Ma et al., 2020). All these factors potentially lead to the obtained k value to be higher on the dayside than on the nightside.

3.3 Preferential Location and Geomagnetic Conditions of Whistler Wave-Driven Precipitation Events

Lastly, we assess where and when electron precipitation events driven by whistler-mode waves occur. Figure 5 shows the occurrence rate and average AE* in an L-MLT map categorized by the precipitation ratio of electrons at 63 keV.

Small ratio events (0.1–0.2) occur quite evenly across L and MLT, with an occurrence rate ranging from ~20% to 40% (Figure 5a), suggesting that both chorus and hiss may drive these small ratio events. For events with a precipitation ratio of 0.2 to 0.4, the occurrence rates decrease to ~5% to 15%, with a preferential occurrence at L > 4 and a peak in the postnoon sector (Figure 5b). This peak is potentially caused by plume hiss, which frequently occurs in the afternoon sector (Chan & Holzer, 1976; R. Shi et al., 2019). For events with higher precipitation ratios (0.4–0.7), the relatively high occurrence rates move to L > 5, peaking from midnight to prenoon and in the afternoon sector with a gap near noon (Figure 5c). This suggests a combined effect of electron precipitation driven by chorus and plume hiss. For large ratio precipitation events greater than 0.7, events are mostly concentrated in the midnight to noon sector at large L shells with a peak occurrence rate below ~5% (Figure 5d), consistent with the global occurrence map of large amplitude chorus (e.g., Li et al., 2011). A small portion of large precipitation events are located in the postnoon sector, may be related to plume hiss. The global occurrence rate distribution sorted by precipitation ratio is mostly consistent with the chorus wave distribution at varying amplitudes (W. Li et al., 2009, 2011) from midnight to noon. Small amplitude chorus waves can be frequently observed in a broad range of L shells and MLTs, while large amplitude chorus waves tend to be concentrated from midnight to pre-noon. However, in the postnoon sector, a high occurrence rate is observed for small to moderate precipitation ratio events (0.2 < Ratio < 0.7) , though it is not contiguous with the chorus wave distribution. This may be due to contributions from other mechanisms, such as precipitation driven by plasmaspheric hiss or plume hiss, or ULF wave modulated precipitation near the flanks (Bashir et al., 2022; Brito et al., 2012, 2015; W. Li et al., 2019; Ma et al., 2021; X. Shi et al., 2022; Yin et al., 2023; W. Zhang et al., 2019).

Figures 5e-5h show the average AE* in each L-MLT bin categorized by the precipitation ratio. Small precipitation ratio (0.1–0.2) events are observed during an average AE* of ~450 nT (Figure 5e). Events with increasing precipitation ratios tend to be observed alongside rising average AE* (Figures 5e-5h). This is consistent with the feature of stronger chorus and hiss wave activity during periods of larger AE*. Moreover, lower L shell electron precipitation events in each category are roughly associated with more intense geomagnetic activity. This trend is observed for events with precipitation ratios of < 0.7, and cannot be concluded for precipitation ratios > 0.7 due to the low sample numbers. As reported, hiss waves are much stronger closer to the edge of the plasmapause ($\Delta L < \sim 2$) and become weaker deep inside the plasmasphere (Malaspina et al., 2016). The plasmasphere will become significantly eroded and move closer to the Earth during intense geomagnetic activity. This may potentially serve to explain the cause of the observed feature that lower L shell electron precipitation is associated with more intense geomagnetic activity.

4 Summary

In this study, we used pitch angle-resolved electron measurements from the dual-probe ELFIN mission at LEO to statistically evaluate the properties of whistler wave driven precipitation, by focusing on their ratio dependence and pitch angle distribution. Our main findings are summarized below.

(a) Large electron precipitation ratio events (at 63 keV), likely driven by intense whistler-mode waves, are associated with high flux outside the loss cone, and extend to higher energies at least up to several hundred keV;

(b) Dayside whistler-mode waves drive larger precipitation ratios at higher energies, extending up to ~500 keV, compared to those on the nightside, likely due to the latitudinal distribution of dayside waves extending to higher latitudes;

(c) Small electron precipitation ratio events are widely distributed across L shells from 3 to 8 at all MLTs, while large electron precipitation ratio events exhibit two peaks at $L > 5$: one from the midnight to prenoon sector, and another in the afternoon. Those two peaks are suggested to be driven by large-amplitude chorus waves and plume hiss, respectively.

(d) Whistler wave-driven precipitation events show a clear dependence on geomagnetic conditions, with larger precipitation ratio events being associated with more intense geomagnetic activity.

Based on the above statistical results and previous studies, we highlight the importance of intense whistler mode waves in driving electron precipitation, especially at higher energies (~hundreds of keV), into the upper atmosphere. Although the occurrence rate of intense whistler waves is much lower than moderate amplitude whistler waves (X.-J. Zhang et al., 2019, 2022), they are found to be correlated with higher trapped flux (e.g., about one order of magnitude higher trapped flux at 63 keV), leading to extremely efficient electron precipitation. Dayside whistler waves are also likely to play an important role in precipitating higher energy electrons potentially due to the fact that dayside whistler waves can extend to higher latitudes, compared to the nightside whistler waves (Meredith et al., 2012).

With assumptions on wave and plasma parameters, including wave normal distribution, wave latitudinal distribution, total electron density, and other parameters, precipitation ratio estimated from only two look directions from the POES satellite has been used to derive global chorus wave distributions (W. Li et al., 2013a; Ni et al., 2014a). A full pitch angle and energy distribution of electron precipitation has the potential to be used to largely advance the capability of inferring global chorus wave distributions from the LEO satellites. Moreover, a fine pitch angle and energy distribution of electron precipitation is crucial for accurately understanding the impact of electron precipitation on the upper atmosphere, as smaller pitch angle inside the loss cone and higher energy electrons may reach lower altitudes.

The obtained slope between the precipitation ratio and electron energy can be applied to electron measurements by LEO satellites, such as POES satellites, which lack a fine energy resolution, to estimate the energy spectra of electron precipitation driven by whistler mode waves.

Acknowledgments

XS, WL, and QM would like to acknowledge the NASA grants 80NSSC20K0698, 80NSSC20K0196, 80NSSC21K1312, 80NSSC20K0704, and 80NSSC24K0572, 80NSSC24K0239, 80NSSC24K0266, and NSF grants AGS-2019950, AGS-2225445, AGS-2247774, AGS-1847818, and AGS-2402179. MH received funding from the Alexander von Humboldt Foundation.

Open Research

Data from the ELFIN is publicly available at NASA's Space Physics Data Facility (ELFIN, 2024). The geomagnetic AE index is from Kyoto University (Nose et al., 2015). We use SPEDAS in IDL to process data files (Angelopoulos et al., 2019). Data to reproduce statistical results in Figures 2, 3, and 5 are made available to the public through Figshare (Shen et al., 2025).

References

Agapitov, O., Mourenas, D., Artemyev, A. V., Mozer, F. S., Hospodarsky, G., Bonnell, J., & Krasnoselskikh, V. (2018). Synthetic Empirical Chorus Wave Model From Combined Van Allen Probes and Cluster Statistics. *Journal of Geophysical Research: Space Physics*, *123*(1), 297–314. https://doi.org/10.1002/2017JA024843

Agapitov, O., Blum, L. W., Mozer, F. S., Bonnell, J. W., & Wygant, J. (2017). Chorus whistler wave source scales as determined from multipoint Van Allen Probe measurements: Chorus Whistler Wave Source Scales. *Geophysical Research Letters*, *44*(6), 2634–2642. https://doi.org/10.1002/2017GL072701

An, X., Artemyev, A., Angelopoulos, V., Zhang, X., Mourenas, D., & Bortnik, J. (2022). Nonresonant Scattering of Relativistic Electrons by Electromagnetic Ion Cyclotron Waves in Earth's Radiation Belts. *Physical Review Letters*, *129*(13), 135101. https://doi.org/10.1103/PhysRevLett.129.135101

Angelopoulos, V., Cruce, P., Drozdov, A., Grimes, E. W., Hatzigeorgiu, N., King, D. A., Larson, D., Lewis, J. W., McTiernan, J. M., Roberts, D. A., Russell, C. L., Hori, T., Kasahara, Y., Kumamoto, A., Matsuoka, A., Miyashita, Y., Miyoshi, Y., Shinohara, I., Teramoto, M., … Schroeder, P. (2019). The Space Physics Environment Data Analysis System (SPEDAS). *Space Science Reviews*, *215*(1), 9. https://doi.org/10.1007/s11214-018-0576-4

Angelopoulos, V., Zhang, X.-J., Artemyev, A. V., Mourenas, D., Tsai, E., Wilkins, C., Runov, A., Liu, J., Turner, D. L., Li, W., Khurana, K., Wirz, R. E., Sergeev, V. A., Meng, X., Wu, J., Hartinger, M. D., Raita, T., Shen, Y., An, X., … Zarifian, A. (2023). Energetic Electron Precipitation Driven by Electromagnetic Ion Cyclotron Waves from ELFIN's Low Altitude Perspective. *Space Science Reviews*, *219*(5), 37. https://doi.org/10.1007/s11214-023-00984-w

Angelopoulos, V., Tsai, E., Bingley, L., Shaffer, C., Turner, D. L., Runov, A., Li, W., Liu, J., Artemyev, A. V., Zhang, X.-J., Strangeway, R. J., Wirz, R. E., Shprits, Y. Y., Sergeev, V. A., Caron, R. P., Chung, M., Cruce, P., Greer, W., Grimes, E., … Zhang, G. Y. (2020). The ELFIN Mission. *Space Science Reviews*, *216*(5), 103. https://doi.org/10.1007/s11214-020-00721-7

Aryan, H., Bortnik, J., Sibeck, D. G., & Hospodarsky, G. (2022). Global Map of Chorus Wave Sizes in the Inner Magnetosphere. *Journal of Geophysical Research: Space Physics*, *127*(3), e2021JA029768. https://doi.org/10.1029/2021JA029768

Bashir, M. F., Artemyev, A., Zhang, X., & Angelopoulos, V. (2022). Energetic Electron Precipitation Driven by the Combined Effect of ULF, EMIC, and Whistler Waves. *Journal of Geophysical Research: Space Physics*, *127*(1). https://doi.org/10.1029/2021JA029871

Blum, L. W., Halford, A., Millan, R., Bonnell, J. W., Goldstein, J., Usanova, M., Engebretson, M., Ohnsted, M., Reeves, G., Singer, H., Clilverd, M., & Li, X. (2015). Observations of coincident EMIC wave activity and duskside energetic electron precipitation on 18-19 January 2013: EMIC Waves and Electron Precipitation. *Geophysical Research Letters*, *42*(14), 5727–5735. https://doi.org/10.1002/2015GL065245

Bortnik, J., Thorne, R. M., & Meredith, N. P. (2008). The unexpected origin of plasmaspheric hiss from discrete chorus emissions. *Nature*, *452*(7183), 62–66. https://doi.org/10.1038/nature06741

Bortnik, J., Li, W., Thorne, R. M., Angelopoulos, V., Cully, C., Bonnell, J., Le Contel, O., & Roux, A. (2009). An Observation Linking the Origin of Plasmaspheric Hiss to Discrete Chorus Emissions. *Science*, *324*(5928), 775–778. https://doi.org/10.1126/science.1171273

Bortnik, J., & Thorne, R. M. (2007). The dual role of ELF/VLF chorus waves in the acceleration and precipitation of radiation belt electrons. *Journal of Atmospheric and Solar-Terrestrial Physics*, *69*(3), 378–386. https://doi.org/10.1016/j.jastp.2006.05.030

Breneman, A. W., Crew, A., Sample, J., Klumpar, D., Johnson, A., Agapitov, O., Shumko, M., Turner, D. L., Santolik, O., Wygant, J. R., Cattell, C. A., Thaller, S., Blake, B., Spence, H., & Kletzing, C. A. (2017). Observations Directly Linking Relativistic Electron Microbursts to Whistler Mode Chorus: Van Allen Probes and FIREBIRD II. *Geophysical Research Letters*, *44*(22), 11,265-11,272. https://doi.org/10.1002/2017GL075001

Brito, T., Woodger, L., Hudson, M., & Millan, R. (2012). Energetic radiation belt electron precipitation showing ULF modulation: ULF WAVES AND RADIATION BELTS. *Geophysical Research Letters*, *39*(22). https://doi.org/10.1029/2012GL053790

Brito, T., Hudson, M. K., Kress, B., Paral, J., Halford, A., Millan, R., & Usanova, M. (2015). Simulation of ULF wave-modulated radiation belt electron precipitation during the 17 March 2013 storm: PRECIPITATION ON MARCH 17 2013. *Journal of Geophysical Research: Space Physics*, *120*(5), 3444–3461. https://doi.org/10.1002/2014JA020838

Capannolo, L., Li, W., Ma, Q., Qin, M., Shen, X.-C., Angelopoulos, V., Artemyev, A., Zhang, X.-J., & Hanzelka, M. (2023). Electron Precipitation Observed by ELFIN Using Proton Precipitation as a Proxy for Electromagnetic Ion Cyclotron (EMIC) Waves. *Geophysical Research Letters*, *50*(21), e2023GL103519. https://doi.org/10.1029/2023GL103519

Capannolo, L., Li, W., Ma, Q., Chen, L., Shen, X. -C., Spence, H. E., Sample, J., Johnson, A., Shumko, M., Klumpar, D. M., & Redmon, R. J. (2019). Direct Observation of Subrelativistic Electron Precipitation Potentially Driven by EMIC Waves. *Geophysical Research Letters*, *46*(22), 12711–12721. https://doi.org/10.1029/2019GL084202

Capannolo, L., Li, W., Ma, Q., Zhang, X. -J., Redmon, R. J., Rodriguez, J. V., Kletzing, C. A., Kurth, W. S., Hospodarsky, G. B., Engebretson, M. J., Spence, H. E., & Reeves, G. D. (2018). Understanding the Driver of Energetic Electron Precipitation Using Coordinated Multisatellite Measurements. *Geophysical Research Letters*, *45*(14), 6755–6765. https://doi.org/10.1029/2018GL078604

Capannolo, L., Li, W., Millan, R., Smith, D., Sivadas, N., Sample, J., & Shekhar, S. (2022). Relativistic Electron Precipitation Near Midnight: Drivers, Distribution, and Properties. *Journal of Geophysical Research: Space Physics*, *127*(1), e2021JA030111. https://doi.org/10.1029/2021JA030111

Chan, K.-W., & Holzer, R. E. (1976). ELF hiss associated with plasma density enhancements in the outer magnetosphere. *Journal of Geophysical Research*, *81*(13), 2267–2274. https://doi.org/10.1029/JA081i013p02267

Chen, L., Bortnik, J., Li, W., Thorne, R. M., & Horne, R. B. (2012). Modeling the properties of plasmaspheric hiss: 1. Dependence on chorus wave emission: HISS SPECTRUM MODELING, 1. *Journal of Geophysical Research: Space Physics*, *117*(A5), n/a-n/a. https://doi.org/10.1029/2011JA017201

Chen, L., Zhang, X.-J., Artemyev, A., Zheng, L., Xia, Z., Breneman, A. W., & Horne, R. B. (2021). Electron Microbursts Induced by Nonducted Chorus Waves. *Frontiers in Astronomy and Space Sciences*, *8*. https://doi.org/10.3389/fspas.2021.745927

Chen, L., Zhang, X.-J., Artemyev, A., Angelopoulos, V., Tsai, E., Wilkins, C., & Horne, R. B. (2022). Ducted Chorus Waves Cause Sub-Relativistic and Relativistic Electron Microbursts. *Geophysical Research Letters*, *49*(5), e2021GL097559. https://doi.org/10.1029/2021GL097559

Chen, L., Thorne, R. M., Bortnik, J., & Zhang, X.-J. (2016). Nonresonant interactions of electromagnetic ion cyclotron waves with relativistic electrons. *Journal of Geophysical Research: Space Physics*, *121*(10), 9913–9925. https://doi.org/10.1002/2016JA022813

Claudepierre, S. G., O'Brien, T. P., Looper, M. D., Blake, J. B., Fennell, J. F., Roeder, J. L., Clemmons, J. H., Mazur, J. E., Turner, D. L., Reeves, G. D., & Spence, H. E. (2019). A Revised Look at Relativistic Electrons in the Earth's Inner Radiation Zone and Slot Region. *Journal of Geophysical Research: Space Physics*, *124*(2), 934–951. https://doi.org/10.1029/2018JA026349

Draganov, A. B., Inan, U. S., Sonwalkar, V. S., & Bell, T. F. (1992). Magnetospherically reflected whistlers as a source of plasmaspheric hiss. *Geophysical Research Letters*, *19*(3), 233–236. https://doi.org/10.1029/91GL03167

ELFIN. (2024). Electron losses and fields investigation (ELFIN) data archive. ELFIN. [Dataset]. Retrieved from https://data.elfin.ucla.edu/

Haiducek, J. D., Ganushkina, N. Y., Dubyagin, S., & Welling, D. T. (2019). The Role of Current Sheet Scattering in the Proton Isotropic Boundary Formation During Geomagnetic Storms. *Journal of Geophysical Research: Space Physics*, *124*(5), 3468–3486. https://doi.org/10.1029/2018JA026290

He, Z., Chen, L., Liu, X., Zhu, H., Liu, S., Gao, Z., & Cao, Y. (2019). Local Generation of High-Frequency Plasmaspheric Hiss Observed by Van Allen Probes. *Geophysical Research Letters*, *46*(3), 1141–1148. https://doi.org/10.1029/2018GL081578

He, Z., Yu, J., Chen, L., Xia, Z., Wang, W., Li, K., & Cui, J. (2020). Statistical Study on Locally Generated High-Frequency Plasmaspheric Hiss and Its Effect on Suprathermal Electrons: Van Allen Probes Observation and Quasi-linear Simulation. *Journal of Geophysical Research: Space Physics*, *125*(10), e2020JA028526. https://doi.org/10.1029/2020JA028526

Horne, R. B., & Thorne, R. M. (2003). Relativistic electron acceleration and precipitation during resonant interactions with whistler-mode chorus: RELATIVISTIC ELECTRON ACCELERATION. *Geophysical Research Letters*, *30*(10). https://doi.org/10.1029/2003GL016973

Jordanova, V. K., Albert, J., & Miyoshi, Y. (2008). Relativistic electron precipitation by EMIC waves from self-consistent global simulations: EMIC WAVES AND RELATIVISTIC

ELECTRONS. *Journal of Geophysical Research: Space Physics*, *113*(A3). https://doi.org/10.1029/2008JA013239

Kim, K.-C., Lee, D.-Y., & Shprits, Y. (2015). Dependence of plasmaspheric hiss on solar wind parameters and geomagnetic activity and modeling of its global distribution. *Journal of Geophysical Research: Space Physics*, *120*(2), 1153–1167. https://doi.org/10.1002/2014JA020687

Li, H., Yuan, Z., Wang, D., Huang, S., Qiao, Z., & Yu, X. (2016). Statistical characteristics of potentially chorus-driven energetic electron precipitation from POES observations. *Journal of Geophysical Research: Space Physics*, *121*(10), 9531–9546. https://doi.org/10.1002/2016JA023101

Li, J., Bortnik, J., An, X., Li, W., Angelopoulos, V., Thorne, R. M., Russell, C. T., Ni, B., Shen, X., Kurth, W. S., Hospodarsky, G. B., Hartley, D. P., Funsten, H. O., Spence, H. E., & Baker, D. N. (2019). Origin of two-band chorus in the radiation belt of Earth. *Nature Communications*, *10*(1), 4672. https://doi.org/10.1038/s41467-019-12561-3

Li, W., Bortnik, J., Thorne, R. M., & Angelopoulos, V. (2011). Global distribution of wave amplitudes and wave normal angles of chorus waves using THEMIS wave observations. *Journal of Geophysical Research: Space Physics*, *116*, A12205. https://doi.org/10.1029/2011JA017035

Li, W., Ni, B., Thorne, R. M., Bortnik, J., Nishimura, Y., Green, J. C., Kletzing, C. A., Kurth, W. S., Hospodarsky, G. B., Spence, H. E., Reeves, G. D., Blake, J. B., Fennell, J. F., Claudepierre, S. G., & Gu, X. (2014). Quantifying hiss-driven energetic electron precipitation: A detailed conjunction event analysis. *Geophysical Research Letters*, *41*(4), 1085–1092. https://doi.org/10.1002/2013GL059132

Li, W., Ni, B., Thorne, R. M., Bortnik, J., Green, J. C., Kletzing, C. A., Kurth, W. S., & Hospodarsky, G. B. (2013a). Constructing the global distribution of chorus wave intensity using measurements of electrons by the POES satellites and waves by the Van Allen Probes: GLOBAL DISTRIBUTION OF CHORUS WAVES. *Geophysical Research Letters*, *40*(17), 4526–4532. https://doi.org/10.1002/grl.50920

Li, W., Shen, X.-C., Ma, Q., Capannolo, L., Shi, R., Redmon, R. J., Rodriguez, J. V., Reeves, G. D., Kletzing, C. A., Kurth, W. S., & Hospodarsky, G. B. (2019). Quantification of Energetic Electron Precipitation Driven by Plume Whistler Mode Waves, Plasmaspheric Hiss, and Exohiss. *Geophysical Research Letters*, *46*(7), 3615–3624. https://doi.org/10.1029/2019GL082095

Li, W., Thorne, R. M., Angelopoulos, V., Bortnik, J., Cully, C. M., Ni, B., LeContel, O., Roux, A., Auster, U., & Magnes, W. (2009). Global distribution of whistler-mode chorus waves observed on the THEMIS spacecraft. *Geophysical Research Letters*, *36*(9), L09104. https://doi.org/10.1029/2009GL037595

Li, W., Thorne, R. M., Bortnik, J., Reeves, G. D., Kletzing, C. A., Kurth, W. S., Hospodarsky, G. B., Spence, H. E., Blake, J. B., Fennell, J. F., Claudepierre, S. G., Wygant, J. R., & Thaller, S. A. (2013b). An unusual enhancement of low-frequency plasmaspheric hiss in the outer plasmasphere associated with substorm-injected electrons. *Geophysical Research Letters*, *40*(15), 3798–3803. https://doi.org/10.1002/grl.50787

Ma, Q., Li, W., Thorne, R. M., Bortnik, J., Kletzing, C. A., Kurth, W. S., & Hospodarsky, G. B. (2016). Electron scattering by magnetosonic waves in the inner magnetosphere. *Journal of Geophysical Research: Space Physics*, *121*(1), 274–285. https://doi.org/10.1002/2015JA021992

Ma, Q., Connor, H. K., Zhang, X. -J., Li, W., Shen, X. -C., Gillespie, D., Kletzing, C. A., Kurth, W. S., Hospodarsky, G. B., Claudepierre, S. G., Reeves, G. D., & Spence, H. E. (2020). Global Survey of Plasma Sheet Electron Precipitation due to Whistler Mode Chorus Waves in Earth's Magnetosphere. *Geophysical Research Letters*, *47*(15). https://doi.org/10.1029/2020GL088798

Ma, Q., Li, W., Zhang, X.-J., Bortnik, J., Shen, X.-C., Connor, H. K., Boyd, A. J., Kurth, W. S., Hospodarsky, G. B., Claudepierre, S. G., Reeves, G. D., & Spence, H. E. (2021). Global Survey of Electron Precipitation due to Hiss Waves in the Earth's Plasmasphere and Plumes. *Journal of Geophysical Research: Space Physics*, *126*(8), e2021JA029644. https://doi.org/10.1029/2021JA029644

Ma, Q., Xu, W., Sanchez, E. R., Marshall, R. A., Bortnik, J., Reyes, P. M., Varney, R. H., Kaeppler, S. R., Miyoshi, Y., Matsuoka, A., Kasahara, Y., Matsuda, S., Tsuchiya, F., Kumamoto, A., Kasahara, S., Yokota, S., Keika, K., Hori, T., Mitani, T., … Tam, S. W.-Y. (2022). Analysis of Electron Precipitation and Ionospheric Density Enhancements Due To Hiss Using Incoherent Scatter Radar and Arase Observations. *Journal of Geophysical Research: Space Physics*, *127*(8), e2022JA030545. https://doi.org/10.1029/2022JA030545

Malaspina, D. M., Jaynes, A. N., Hospodarsky, G., Bortnik, J., Ergun, R. E., & Wygant, J. (2017). Statistical properties of low-frequency plasmaspheric hiss. *Journal of Geophysical Research: Space Physics*, *122*(8), 8340–8352. https://doi.org/10.1002/2017JA024328

Malaspina, D. M., Jaynes, A. N., Boulé, C., Bortnik, J., Thaller, S. A., Ergun, R. E., Kletzing, C. A., & Wygant, J. R. (2016). The distribution of plasmaspheric hiss wave power with respect to plasmapause location. *Geophysical Research Letters*, *43*(15), 7878–7886. https://doi.org/10.1002/2016GL069982

Meredith, N. P., Horne, R. B., & Anderson, R. R. (2001). Substorm dependence of chorus amplitudes: Implications for the acceleration of electrons to relativistic energies. *Journal of Geophysical Research: Space Physics*, *106*(A7), 13165–13178. https://doi.org/10.1029/2000JA900156

Meredith, N. P., Horne, R. B., Clilverd, M. A., Horsfall, D., Thorne, R. M., & Anderson, R. R. (2006). Origins of plasmaspheric hiss. *Journal of Geophysical Research: Space Physics*, *111*(A9). https://doi.org/10.1029/2006JA011707

Meredith, N. P., Horne, R. B., Shen, X.-C., Li, W., & Bortnik, J. (2020). Global Model of Whistler Mode Chorus in the Near-Equatorial Region (|λm|< 18°). *Geophysical Research Letters*, *47*(11). https://doi.org/10.1029/2020GL087311

Meredith, N. P., Bortnik, J., Horne, R. B., Li, W., & Shen, X.-C. (2021). Statistical Investigation of the Frequency Dependence of the Chorus Source Mechanism of Plasmaspheric Hiss. *Geophysical Research Letters*, *48*(6). https://doi.org/10.1029/2021GL092725

Meredith, N. P., Horne, R. B., Sicard-Piet, A., Boscher, D., Yearby, K. H., Li, W., & Thorne, R. M. (2012). Global model of lower band and upper band chorus from multiple satellite observations: GLOBAL MODEL OF WHISTLER MODE CHORUS. *Journal of Geophysical Research: Space Physics*, *117*(A10). https://doi.org/10.1029/2012JA017978

Meredith, N. P., Horne, R. B., Kersten, T., Li, W., Bortnik, J., Sicard, A., & Yearby, K. H. (2018). Global Model of Plasmaspheric Hiss From Multiple Satellite Observations. *Journal of Geophysical Research: Space Physics*, *123*(6), 4526–4541. https://doi.org/10.1029/2018JA025226

Miyoshi, Y., Sakaguchi, K., Shiokawa, K., Evans, D., Albert, J., Connors, M., & Jordanova, V. (2008). Precipitation of radiation belt electrons by EMIC waves, observed from ground and space. *Geophysical Research Letters*, *35*(23), L23101. https://doi.org/10.1029/2008GL035727

Nose M., Iyemori T., Sugiura M. and Kamei T. (2015). Geomagnetic AE index [Dataset]. *World Data Center for Geomagnetism*. doi:10.17593/15031-54800.

Ni, B., Thorne, R. M., Shprits, Y. Y., & Bortnik, J. (2008). Resonant scattering of plasma sheet electrons by whistler-mode chorus: Contribution to diffuse auroral precipitation. *Geophysical Research Letters*, *35*(11), L11106. https://doi.org/10.1029/2008GL034032

Ni, B., Li, W., Thorne, R. M., Bortnik, J., Green, J. C., Kletzing, C. A., Kurth, W. S., Hospodarsky, G. B., & de Soria-Santacruz Pich, M. (2014a). A novel technique to construct the global distribution of whistler mode chorus wave intensity using low-altitude POES electron data: A novel technique for global wave model. *Journal of Geophysical Research: Space Physics*, *119*(7), 5685–5699. https://doi.org/10.1002/2014JA019935

Ni, B., Bortnik, J., Nishimura, Y., Thorne, R. M., Li, W., Angelopoulos, V., Ebihara, Y., & Weatherwax, A. T. (2014b). Chorus wave scattering responsible for the Earth's dayside diffuse auroral precipitation: A detailed case study. *Journal of Geophysical Research: Space Physics*, *119*(2), 897–908. https://doi.org/10.1002/2013JA019507

Nishimura, Y., Bortnik, J., Li, W., Thorne, R. M., Lyons, L. R., Angelopoulos, V., Mende, S. B., Bonnell, J. W., Le Contel, O., Cully, C., Ergun, R., & Auster, U. (2010). Identifying the Driver of Pulsating Aurora. *Science*, *330*(6000), 81–84. https://doi.org/10.1126/science.1193186

Omura, Y., & Zhao, Q. (2012). Nonlinear pitch angle scattering of relativistic electrons by EMIC waves in the inner magnetosphere: ELECTRON PRECIPITATION BY EMIC WAVES. *Journal of Geophysical Research: Space Physics*, *117*(A8). https://doi.org/10.1029/2012JA017943

Ozaki, M., Shiokawa, K., Miyoshi, Y., Hosokawa, K., Oyama, S., Yagitani, S., Kasahara, Y., Kasaba, Y., Matsuda, S., Kataoka, R., Ebihara, Y., Ogawa, Y., Otsuka, Y., Kurita, S., Moore, R. C., Tanaka, Y. -M., Nosé, M., Nagatsuma, T., Connors, M., … Shinohara, I. (2018). Microscopic Observations of Pulsating Aurora Associated With Chorus Element Structures: Coordinated Arase Satellite-PWING Observations. *Geophysical Research Letters*, *45*(22), 12,125-12,134. https://doi.org/10.1029/2018GL079812

Ozaki, M., Miyoshi, Y., Shiokawa, K., Hosokawa, K., Oyama, S., Kataoka, R., Ebihara, Y., Ogawa, Y., Kasahara, Y., Yagitani, S., Kasaba, Y., Kumamoto, A., Tsuchiya, F., Matsuda, S., Katoh, Y., Hikishima, M., Kurita, S., Otsuka, Y., Moore, R. C., … Shinohara, I. (2019). Visualization of rapid electron precipitation via chorus element wave–particle interactions. *Nature Communications*, *10*(1), 257. https://doi.org/10.1038/s41467-018-07996-z

Qin, M., Hudson, M., Millan, R., Woodger, L., & Shekhar, S. (2018). Statistical Investigation of the Efficiency of EMIC Waves in Precipitating Relativistic Electrons. *Journal of Geophysical Research: Space Physics*, *123*(8), 6223–6230. https://doi.org/10.1029/2018JA025419

Qin, M., Hudson, M., Millan, R., Woodger, L., & Shen, X. (2020). Statistical Dependence of EMIC Wave Scattering on Wave and Plasma Parameters. *Journal of Geophysical Research: Space Physics*, *125*(4), e2020JA027772. https://doi.org/10.1029/2020JA027772

Sergeev, V. A., Sazhina, E. M., Tsyganenko, N. A., Lundblad, J. Å., & Søraas, F. (1983). Pitch-angle scattering of energetic protons in the magnetotail current sheet as the dominant source of their isotropic precipitation into the nightside ionosphere. *Planetary and Space Science*, *31*(10), 1147–1155. https://doi.org/10.1016/0032-0633(83)90103-4

Shen, X.-C., Li, W., Ma, Q., Qin, M., Capannolo, L., Hanzelka, M., Huang, S., & Chu, X. (2024). Large Amplitude Whistler Waves in Earth's Plasmasphere and Plasmaspheric Plumes. *Geophysical Research Letters*, *51*(8), e2023GL105244. https://doi.org/10.1029/2023GL105244

Shen, X.-C., Li, W., Capannolo, L., Ma, Q., Qin, M., Artemyev, A. V., Angelopoulos, V., Zhang, X.-J., & Huang, S. (2023). Modulation of Energetic Electron Precipitation Driven by Three Types of Whistler Mode Waves. *Geophysical Research Letters*, *50*(8), e2022GL101682. https://doi.org/10.1029/2022GL101682

Shen, X.-C., Li, W., Ma, Q., Agapitov, O., & Nishimura, Y. (2019). Statistical Analysis of Transverse Size of Lower Band Chorus Waves Using Simultaneous Multisatellite Observations. *Geophysical Research Letters*, *46*(11), 5725–5734. https://doi.org/10.1029/2019GL083118

Shen, X.-C., Hudson, M. K., Jaynes, A. N., Shi, Q., Tian, A., Claudepierre, S. G., Qin, M.-R., Zong, Q.-G., & Sun, W.-J. (2017). Statistical study of the storm time radiation belt evolution during Van Allen Probes era: CME- versus CIR-driven storms: Radiation Belt Electron Evolution. *Journal of Geophysical Research: Space Physics*, *122*(8), 8327–8339. https://doi.org/10.1002/2017JA024100

Shen, X.-C., Li, W., Ma, Q., Qin, M., Capannolo, L., Hanzelka, M., Angelopoulos, V., Artemyev, A., Wilkins, C., Liu J., Tsai, E. (2025). Dataset for Whistler Mode Wave-Driven Electron Scattering Properties from ELFIN Measurements of the Precipitation Ratio. *Figshare*, https://doi.org/10.6084/m9.figshare.28603769

Shi, R., Li, W., Ma, Q., Green, A., Kletzing, C. A., Kurth, W. S., Hospodarsky, G. B., Claudepierre, S. G., Spence, H. E., & Reeves, G. D. (2019). Properties of Whistler Mode Waves in Earth's Plasmasphere and Plumes. *Journal of Geophysical Research: Space Physics*, *124*(2), 1035–1051. https://doi.org/10.1029/2018JA026041

Shi, X., Zhang, X.-J., Artemyev, A., Angelopoulos, V., Hartinger, M. D., Tsai, E., & Wilkins, C. (2022). On the Role of ULF Waves in the Spatial and Temporal Periodicity of Energetic Electron Precipitation. *Journal of Geophysical Research: Space Physics*, *127*(12), e2022JA030932. https://doi.org/10.1029/2022JA030932

Shumko, M., Sample, J., Johnson, A., Blake, B., Crew, A., Spence, H., Klumpar, D., Agapitov, O., & Handley, M. (2018). Microburst Scale Size Derived From Multiple Bounces of a Microburst Simultaneously Observed With the FIREBIRD-II CubeSats. *Geophysical Research Letters*, *45*(17), 8811–8818. https://doi.org/10.1029/2018GL078925

Wilkins, C., Angelopoulos, V., Runov, A., Artemyev, A., Zhang, X.-J., Liu, J., & Tsai, E. (2023). Statistical Characteristics of the Electron Isotropy Boundary. *Journal of Geophysical Research: Space Physics*, *128*(10), e2023JA031774. https://doi.org/10.1029/2023JA031774

Yin, Z.-F., Zhou, X.-Z., Li, W., Shen, X.-C., Rankin, R., Liu, J., Hu, Z.-J., Liu, J.-J., Zong, Q.-G., Li, L., & Wang, Y.-F. (2023). Characteristics of Electron Precipitation Directly Driven by Poloidal ULF Waves. *Journal of Geophysical Research: Space Physics*, *128*(3), e2022JA031163. https://doi.org/10.1029/2022JA031163

Yue, C., Wang, C.-P., Lyons, L., Liang, J., Donovan, E. F., Zaharia, S. G., & Henderson, M. (2014). Current sheet scattering and ion isotropic boundary under 3-D empirical force-balanced magnetic field. *Journal of Geophysical Research: Space Physics*, *119*(10), 8202–8211. https://doi.org/10.1002/2014JA020172

Zhang, S., Rae, I. J., Watt, C. E. J., Degeling, A. W., Tian, A., Shi, Q., Shen, X.-C., Yao, S., Guo, R., Wang, M., Zhu, X., & Wang, H. (2021). Determining the Global Scale Size of Chorus Waves in the Magnetosphere. *Journal of Geophysical Research: Space Physics*, *126*(11), e2021JA029569. https://doi.org/10.1029/2021JA029569

Zhang, W., Ni, B., Huang, H., Summers, D., Fu, S., Xiang, Z., Gu, X., Cao, X., Lou, Y., & Hua, M. (2019). Statistical Properties of Hiss in Plasmaspheric Plumes and Associated Scattering Losses of Radiation Belt Electrons. *Geophysical Research Letters*, *46*(11), 5670–5680. https://doi.org/10.1029/2018GL081863

Zhang, X.-J., Mourenas, D., Shen, X.-C., Qin, M., Artemyev, A. V., Ma, Q., Li, W., Hudson, M. K., & Angelopoulos, V. (2021). Dependence of Relativistic Electron Precipitation in the Ionosphere on EMIC Wave Minimum Resonant Energy at the Conjugate Equator. *Journal of Geophysical Research: Space Physics*, *126*(5), e2021JA029193. https://doi.org/10.1029/2021JA029193

Zhang, X.-J., Mourenas, D., Artemyev, A. V., Angelopoulos, V., Bortnik, J., Thorne, R. M., Kurth, W. S., Kletzing, C. A., & Hospodarsky, G. B. (2019). Nonlinear Electron Interaction With Intense Chorus Waves: Statistics of Occurrence Rates. *Geophysical Research Letters*, *46*(13), 7182–7190. https://doi.org/10.1029/2019GL083833

Zhang, X.-J., Artemyev, A., Angelopoulos, V., Tsai, E., Wilkins, C., Kasahara, S., Mourenas, D., Yokota, S., Keika, K., Hori, T., Miyoshi, Y., Shinohara, I., & Matsuoka, A. (2022). Superfast precipitation of energetic electrons in the radiation belts of the Earth. *Nature Communications*, *13*(1), 1611. https://doi.org/10.1038/s41467-022-29291-8

Zhao, H., Ni, B., Li, X., Baker, D. N., Johnston, W. R., Zhang, W., Xiang, Z., Gu, X., Jaynes, A. N., Kanekal, S. G., Blake, J. B., Claudepierre, S. G., Temerin, M. A., Funsten, H. O., Reeves, G. D., & Boyd, A. J. (2019). Plasmaspheric hiss waves generate a reversed energy spectrum of radiation belt electrons. *Nature Physics*, *15*(4), 367–372. https://doi.org/10.1038/s41567-018-0391-6

Figures and Captions

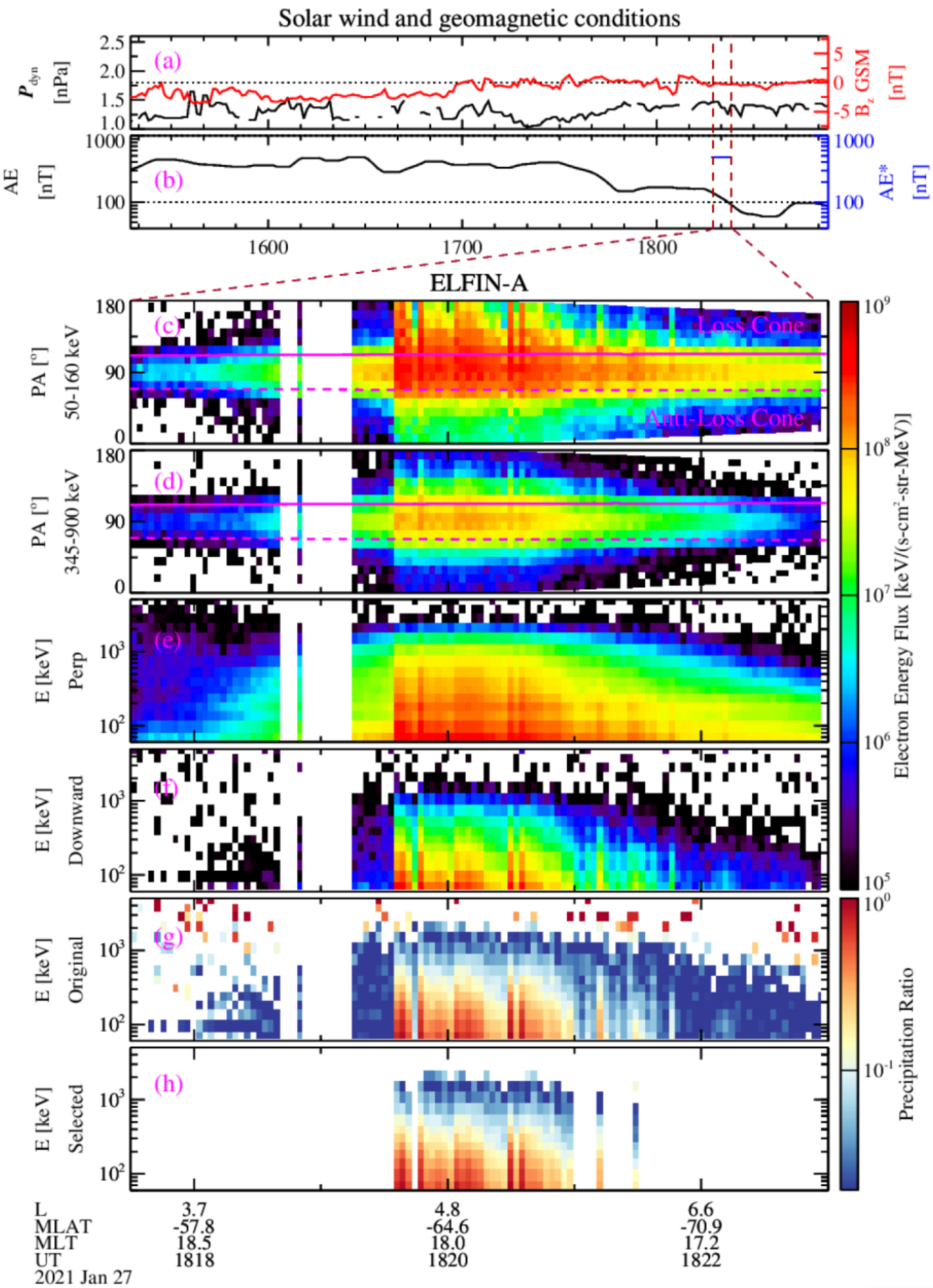

Figure 1. Overview of solar wind and geomagnetic conditions from the OMNI dataset and electron flux observed by ELFIN-A. (a) Solar wind dynamic pressure (black) and interplanetary magnetic field (IMF) B_z component (red) in GSM coordinates. (b) Geomagnetic AE (black) and AE* (maximum value in the preceding three hours; blue) index. (c–d) Pitch angle distribution of 50–160 keV and 345–900 keV electrons, respectively. (e–f) Energy spectrogram of trapped and precipitating electron energy flux. (g) Energy spectrogram of electron precipitation ratio (calculated as the average precipitating energy flux divided by the average trapped energy flux). (h) Selected electron precipitation ratio driven by whistler mode waves.

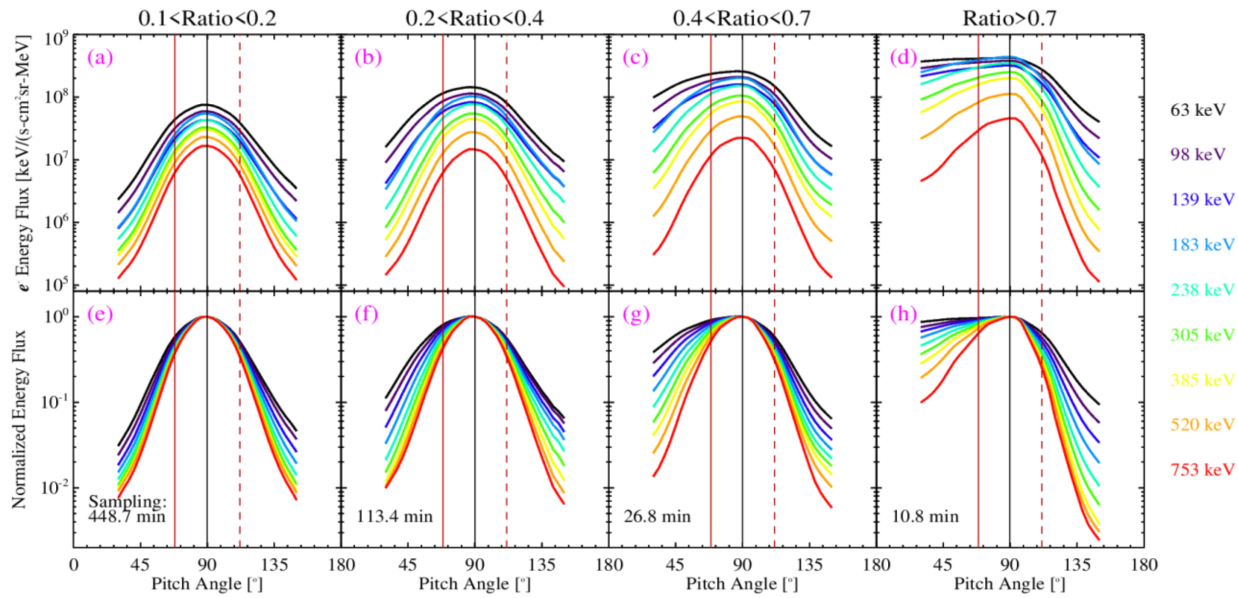

Figure 2. Statistical results of whistler wave-driven electron pitch angle distributions from the ELFIN observations. (a–d) Median pitch angle distributions of electron energy flux for events with a precipitation ratio at 63 keV from 0.1 to 0.2, from 0.2 to 0.4, from 0.4 to 0.7, and larger than 0.7, respectively color coded for various energies from 63 keV to 753 keV. (e-h) Same format as (a-d) but for the pitch angle distributions divided by the flux at 90° pitch angle in each energy channel.

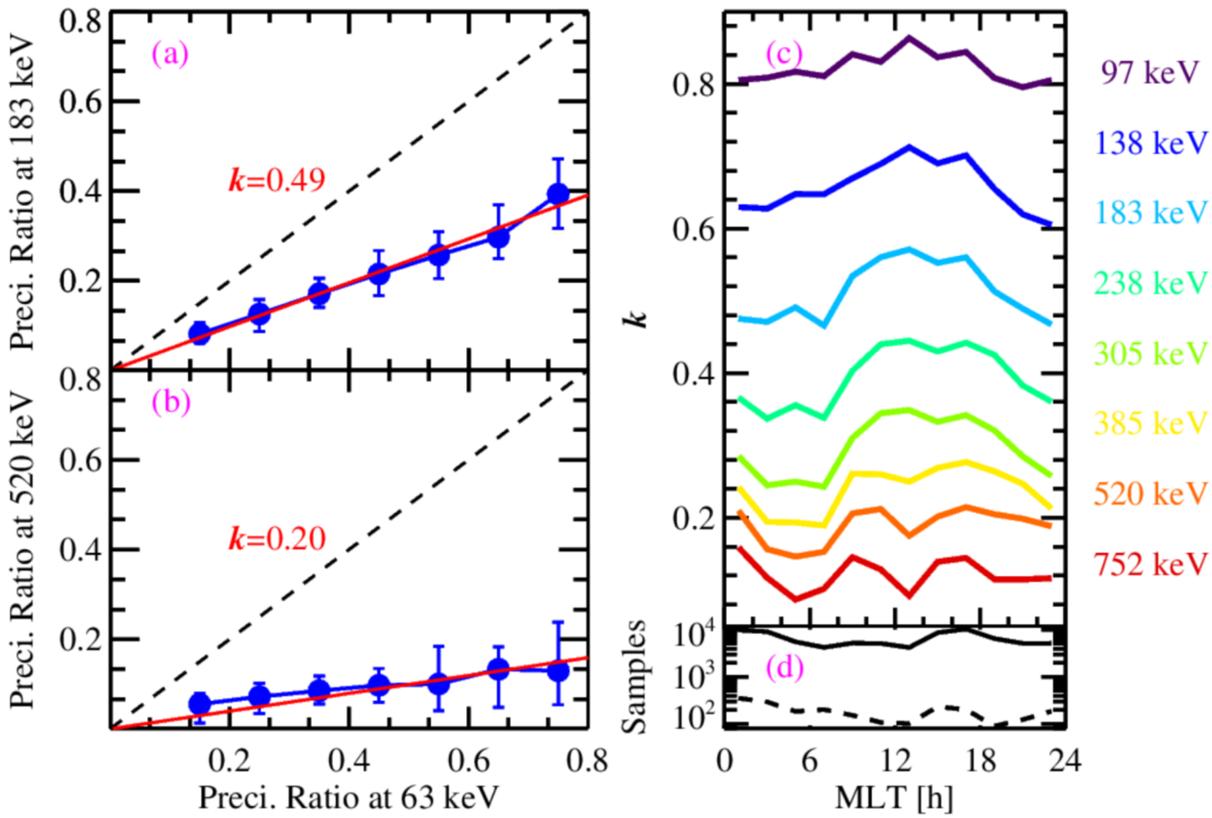

Figure 3. Relation of precipitation ratios between different energies. (a) Median (blue dotted line) and quartiles (error bar) of precipitation ratio at 183 keV as a function of precipitation ratio at 63 keV. The red line illustrates the linear fitting of the median values with its slope *k* marked on the panel. Black dashed line represents a slope value of 1 for reference. (b) Similar to panel (a) but for 520 keV. (c) Fitted slope value *k* as a function of MLT color coded for various energies. (d) Number of samples (each sample is one half spin measurement, ~1.5 s) for precipitation events with a moderate precipitation ratio (0.1 – 0.6; solid line) and precipitation events with an intense precipitation ratio (0.6 – 0.8; dashed line).

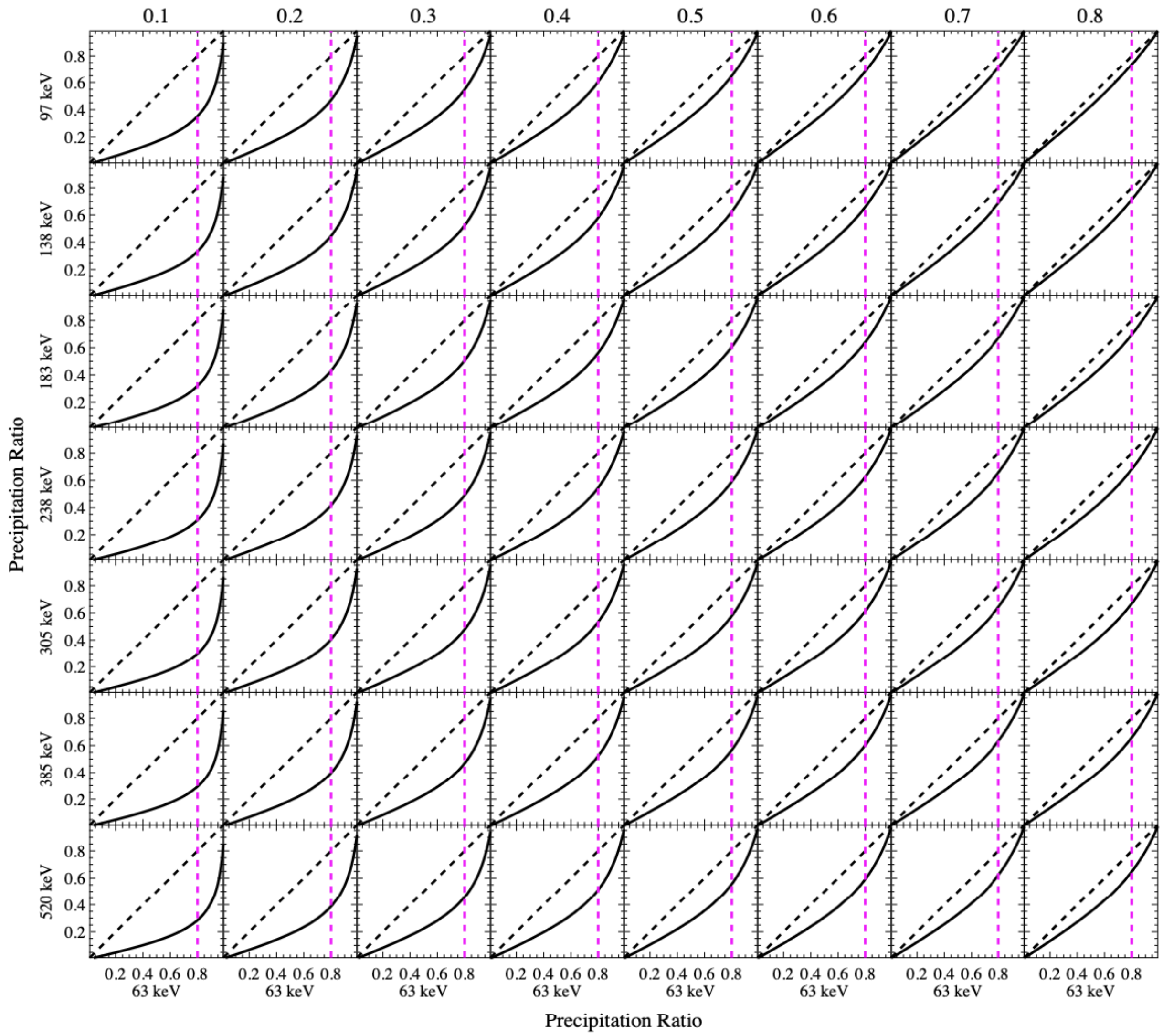

Figure 4. Relation between precipitation ratios at > 63 keV energy channels and 63 keV electrons estimated from the quasi-linear theory. Top to bottom rows are for different energy channels from 97 keV to 520 keV, corresponding to the ELFIN energy channels. The left to right columns are for different ratios of $<\boldsymbol{D_{\alpha\alpha|E_{high}}}>/<\boldsymbol{D_{\alpha\alpha|63\ keV}}>$, where $\boldsymbol{E_{high}}$ is the selected energy channel marked to the left of each row. The black dashed line in each panel indicates a slope of one; the magenta dashed line in each panel marks the precipitation ratio of 63 keV electrons to be 0.8.

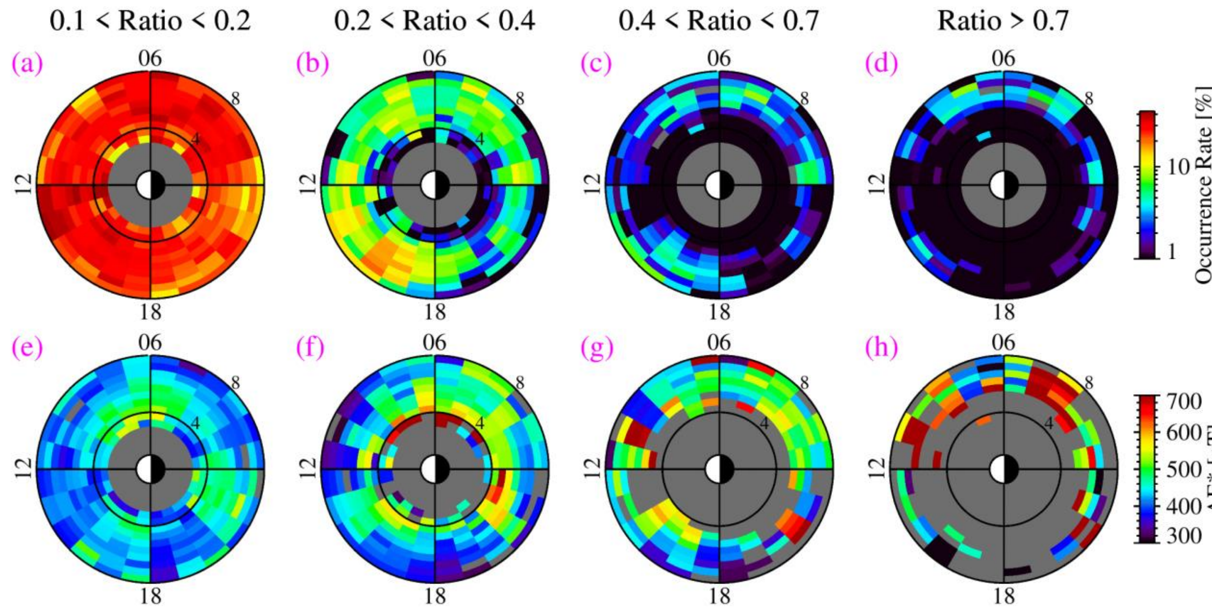

Figure 5. Occurrence rate (top) and average AE* (bottom) of whistler wave-driven precipitation events sorted by precipitation ratio at 63 keV. (a-d) Occurrence rate of whistler wave-driven electron precipitation events in the L-MLT coordinates with a precipitation ratio of 0.1–0.2, 0.2–0.4, 0.4–0.7, and > 0.7, respectively. (e-f) Same format as panels (a-d) but for average AE*.

Figure 1.

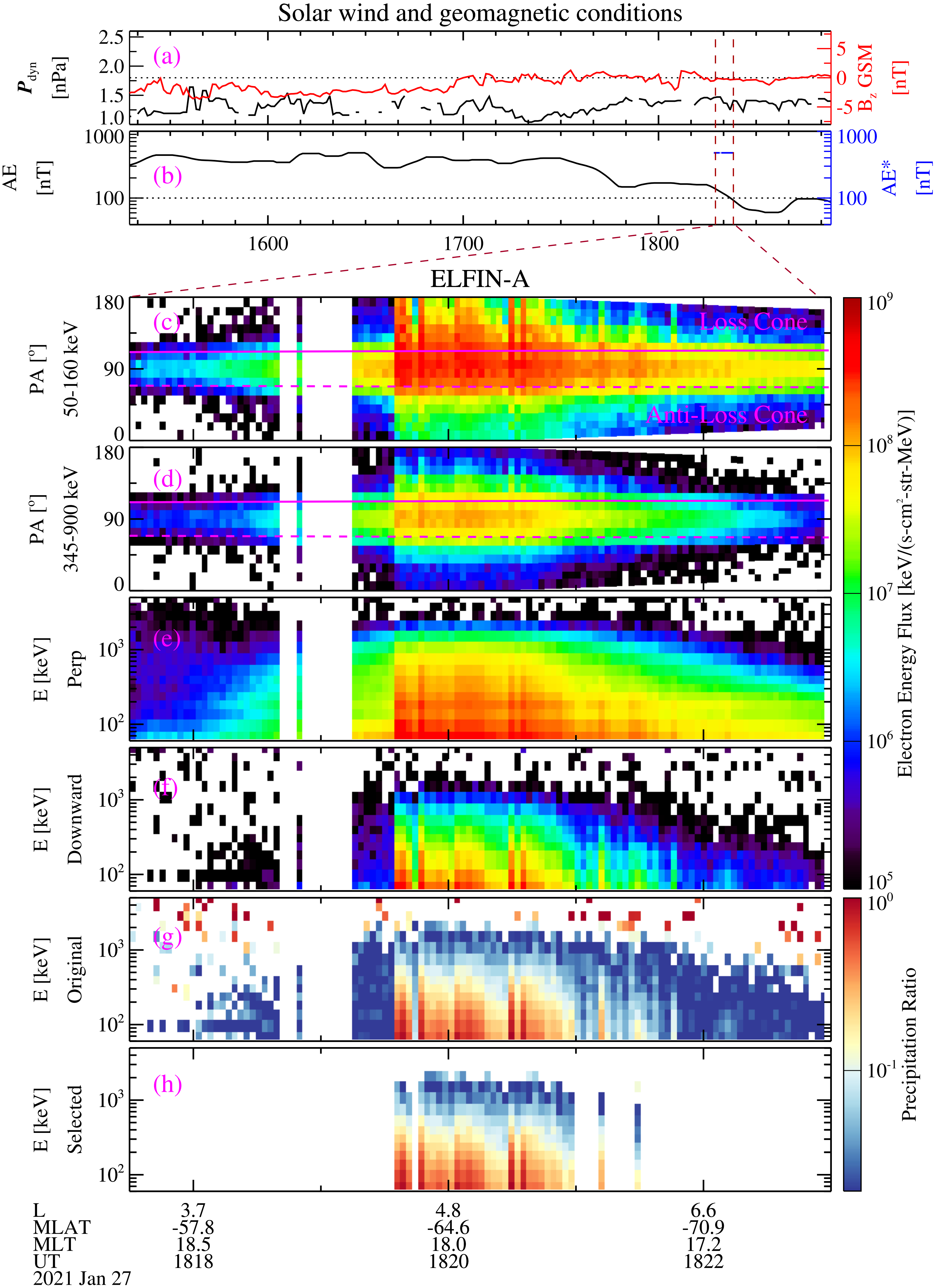

Solar wind and geomagnetic conditions
(a)
P_dyn [nPa]
B_z GSM [nT]
(b)
AE [nT]
AE* [nT]
ELFIN-A
(c)
Loss Cone
Anti-Loss Cone
PA [°] 50-160 keV
(d)
PA [°] 345-900 keV
(e)
E [keV] Perp
(f)
E [keV] Downward
(g)
E [keV] Original
(h)
E [keV] Selected
Electron Energy Flux [keV/(s-cm²-str-MeV)]
Precipitation Ratio
L 3.7 4.8 6.6
MLAT -57.8 -64.6 -70.9
MLT 18.5 18.0 17.2
UT 1818 1820 1822
2021 Jan 27

Figure 2.

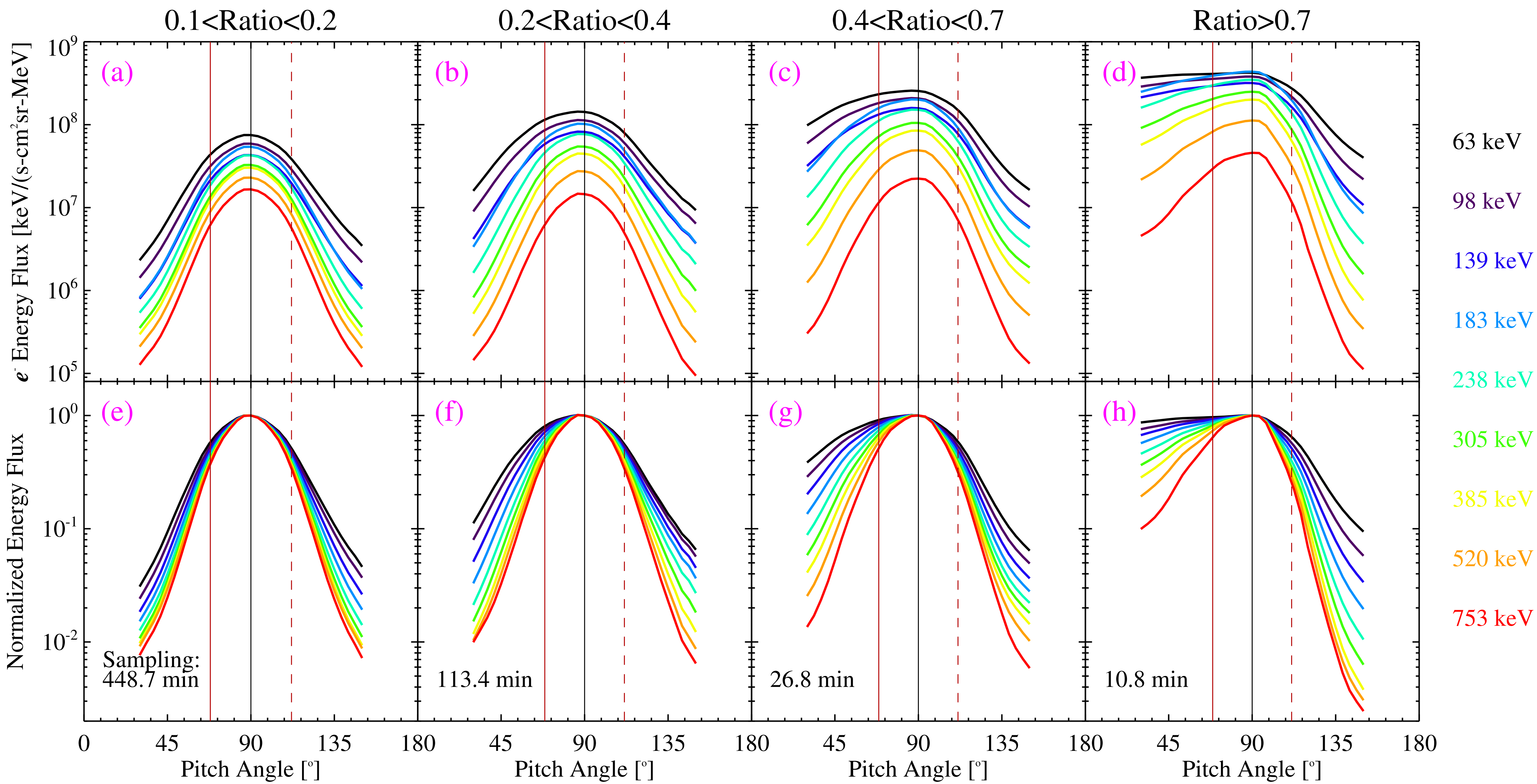
0.1<Ratio<0.2
0.2<Ratio<0.4
0.4<Ratio<0.7
Ratio>0.7
(a)
(b)
(c)
(d)
(e)
(f)
(g)
(h)
e⁻ Energy Flux [keV/(s-cm²sr-MeV]
Normalized Energy Flux
Sampling: 448.7 min
113.4 min
26.8 min
10.8 min
Pitch Angle [°]
63 keV
98 keV
139 keV
183 keV
238 keV
305 keV
385 keV
520 keV
753 keV

Figure 3.

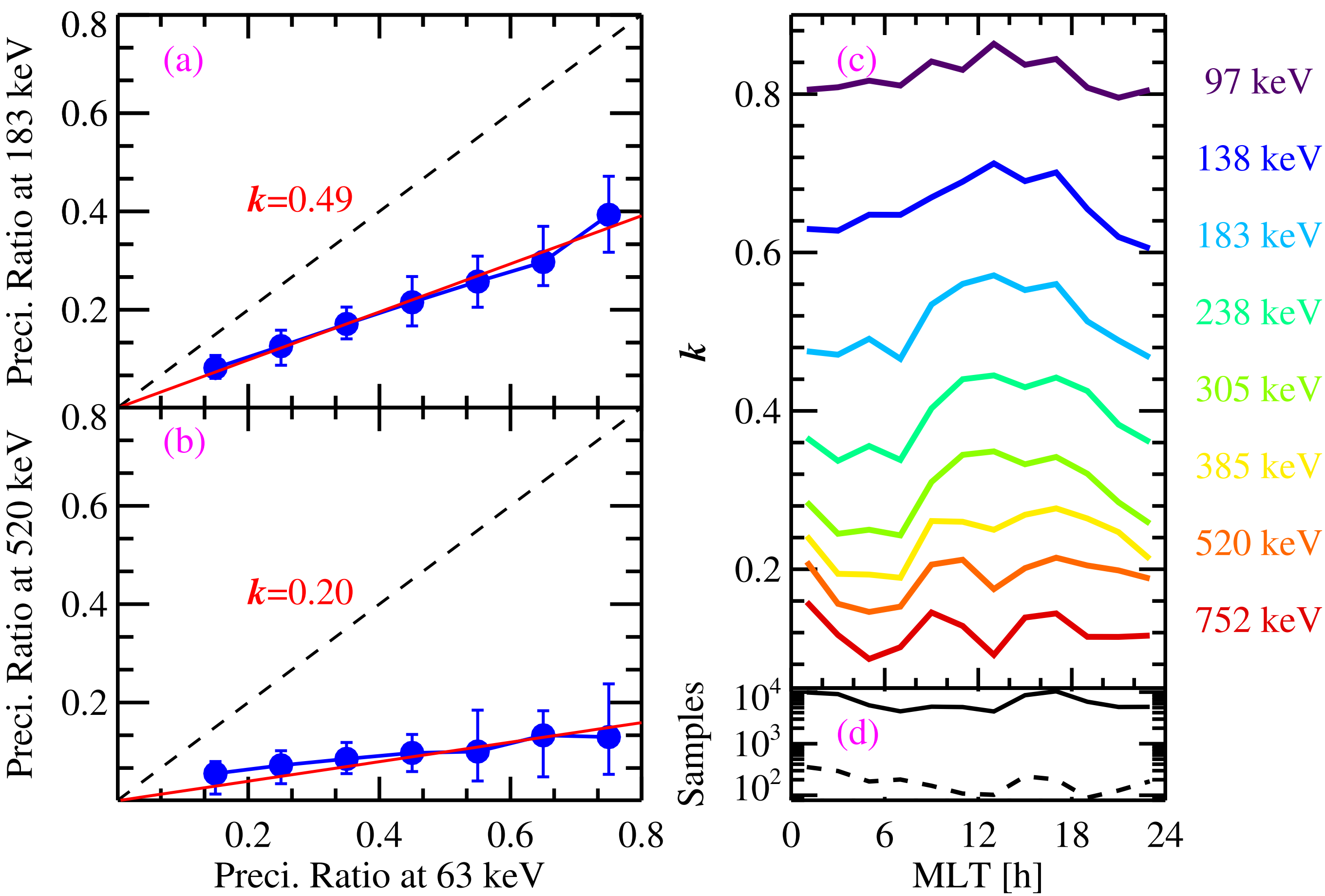
(a)
k=0.49
Preci. Ratio at 183 keV
(b)
k=0.20
Preci. Ratio at 520 keV
Preci. Ratio at 63 keV
0.2
0.4
0.6
0.8
(c)
k
97 keV
138 keV
183 keV
238 keV
305 keV
385 keV
520 keV
752 keV
(d)
Samples
10^4
10^3
10^2
0
6
12
18
24
MLT [h]

Figure 4.

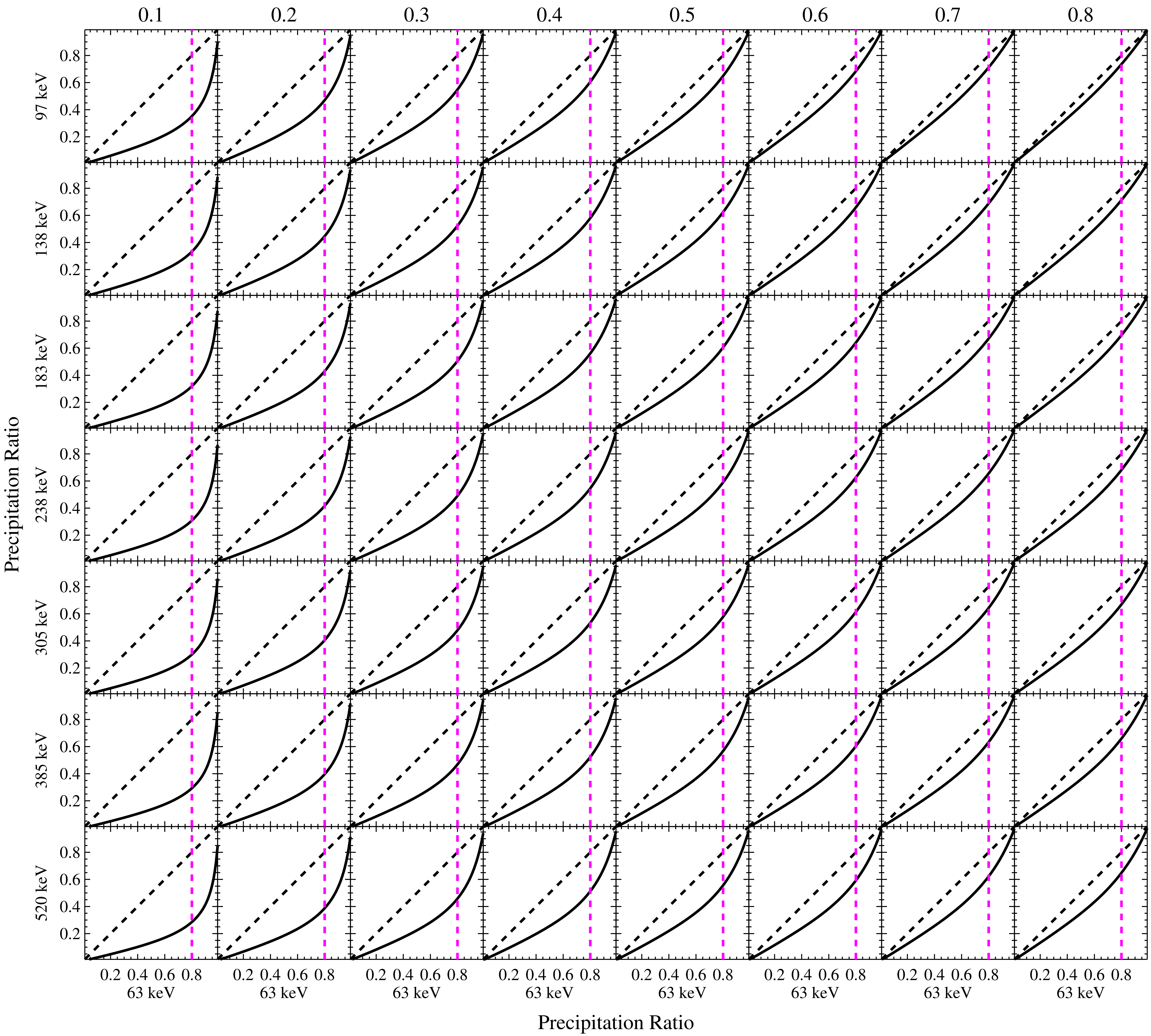

0.1
0.2
0.3
0.4
0.5
0.6
0.7
0.8
97 keV
138 keV
183 keV
238 keV
305 keV
385 keV
520 keV
0.2 0.4 0.6 0.8
63 keV
Precipitation Ratio
Precipitation Ratio

Figure 5.

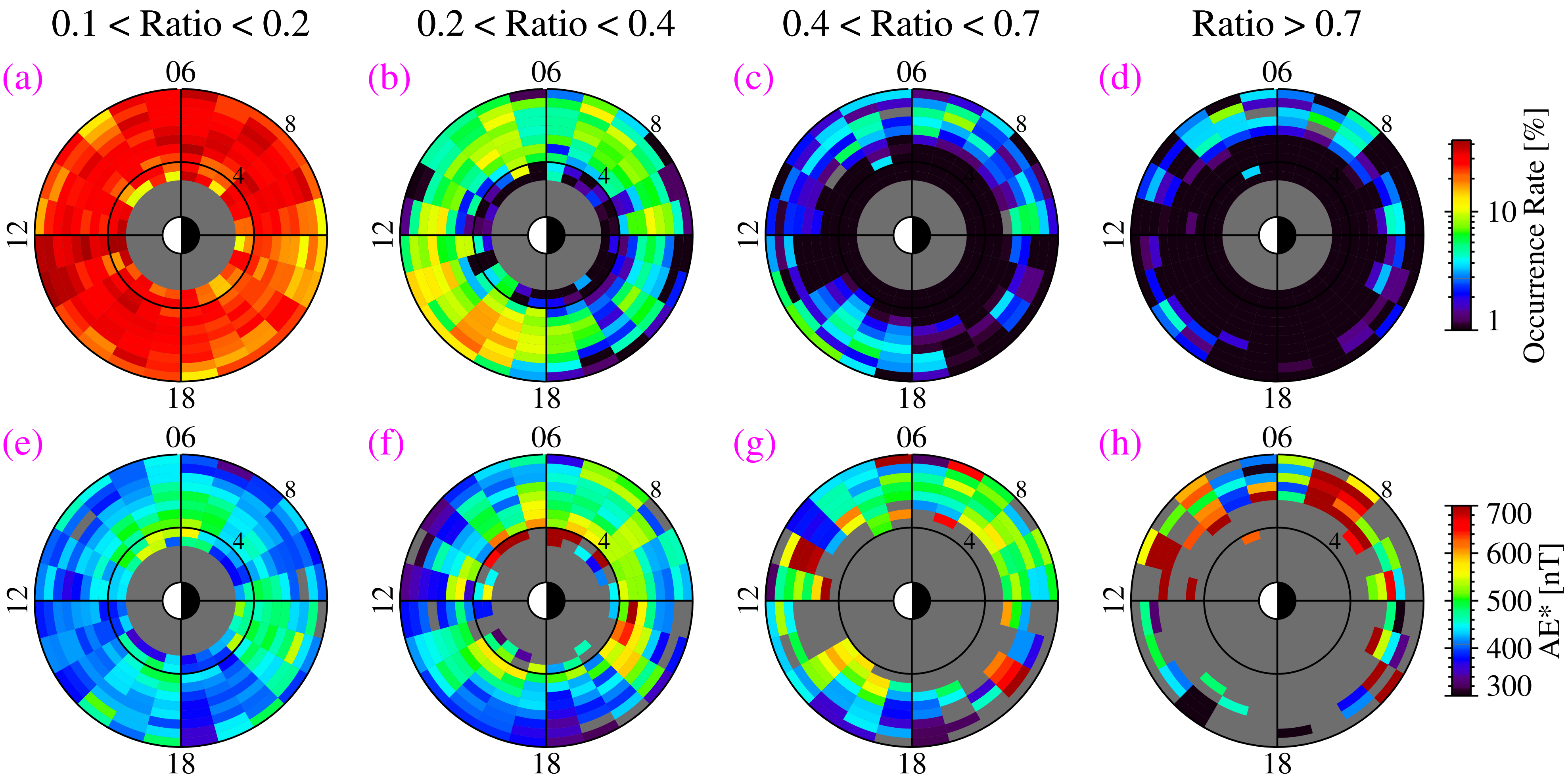
0.1 < Ratio < 0.2
0.2 < Ratio < 0.4
0.4 < Ratio < 0.7
Ratio > 0.7
(a)
(b)
(c)
(d)
(e)
(f)
(g)
(h)
06
12
18
8
4
Occurrence Rate [%]
10
1
AE* [nT]
700
600
500
400
300